Novel $Bi_2Sn_2O_7$ quantum dots/TiO_2 nanotube arrays S-scheme heterojunction for enhanced photoelectrocatalytic degradation of sulfamethazine

Huizhong Wu [a,b], Zhongzheng Hu [a,b], Ruiheng Liang [a,b], Oluchi V. Nkwachukwu [c,d], Omotayo A. Arotiba [c,d], Minghua Zhou [a,b,*]

[a] *Tianjin Key Laboratory of Environmental Technology for Complex Trans-Media Pollution, College of Environmental Science and Engineering, Nankai University, Tianjin 300350, China*
[b] *Tianjin Advanced Water Treatment Technology International Joint Research Center, College of Environmental Science and Engineering, Nankai University, Tianjin 300350, China*
[c] *Department of Chemical Sciences, University of Johannesburg, Doornfontein 2028, South Africa*
[d] *Centre for Nanomaterials Science Research, University of Johannesburg, South Africa*

ARTICLE INFO

ABSTRACT

The step-scheme (S-scheme) heterojunction of $Bi_2Sn_2O_7$ quantum dots (QDs)/TiO_2 nanotube arrays (NTAs) photoanodes were prepared for efficient and stable photoelectrocatalytic (PEC) degradation of sulfamethazine (SMT) at low potential and light-emitting diode (LED) illumination. In the $Bi_2Sn_2O_7$/TiO_2 NTAs system, the synergistic factor of photocatalysis (PC) and electrocatalysis (EC) reached 10.1. The elevated performance was attributed to improved light-harvest capability by the decorated TiO_2 NTAs with $Bi_2Sn_2O_7$ QDs, lower charge transfer resistance, more efficient photoexcited charge separation, and higher redox ability to produce photo-generated holes (h^+) and reactive oxygen species (ROS) with great efficiency. The possible PEC mechanism of S-scheme $Bi_2Sn_2O_7$/TiO_2 NTAs was elucidated by experimental studies and density functional theory (DFT) calculations, which confirmed the establishment of the internal electric field (IEF) promoted carrier separation and transport. This research provides a feasible approach for fabricating superior PEC photoanodes as well as new insights into heterojunction design.

1. Introduction

Sulfamethazine (SMT), a common sulfonamide bacteriostatic antibiotic, is widely present in the sediment, soil, rivers, and groundwater[1, 2]. Unfortunately, traditional water treatment technologies including adsorption, coagulation, and filtration are inefficient at eliminating SMT from contaminated water[3]. Therefore, developing a cost-effective and ecologically friendly treatment procedure to effectively remove SMT is critical.

In terms of utilizing renewable solar energy, high degradation capacity, mild reaction conditions, and effective catalyst recovery, photoelectrocatalysis (PEC) has demonstrated enormous potential in pollutant degradation as one of the emerging advanced oxidation processes (AOPs)[4–6]. A light-harvesting electrode, a counter electrode,

and an electrolyte capable of carrying electricity make up a conventional PEC cell. In the PEC process, light irradiation and external potential effectively separate the charge pairs to the cathode and anode, providing an ideal method for achieving various photoelectrochemical conversions, including degradation of water contaminants by generating reactive oxygen species (ROS) and reducing protons or water to hydrogen molecules [7,8]. Notably, the light source we employ is a light-emitting diode (LED) lamp with lower energy consumption, less toxicity, and a longer lifetime compared to other simulated light sources (such as Xe and Hg lamps)[9,10]. When irradiated with sufficiently intense light, the photoanode creates electrons (e^-) with a strong reducing ability and h^+ with a strong oxidizing ability; nevertheless, the photo-induced carriers of this instability excited state are easily recombined. Fortunately, the employed constant anode potential allows

for charge carrier orientation separation and transfer. Through the external circuit, e^- from the semiconductor's conduction band (CB) can travel to the counter electrode, thus suppressing the recombination of e^- - h^+ pairs. The h^+ in the valence band (VB) of the photoanode can react with H_2O to create $\bullet OH$, which can then be used to oxidize pollutants or directly oxidize pollutants. Moreover, due to the external circuit, holes (positive charge) are transferred to the photoanode, which results in more $\bullet OH$ production at the photoanode.

PEC can better restrict the recombination of photogenerated carriers by applying an external potential compared with photocatalysis (PC), thus boosting the degradation efficiency. When compared to electrocatalysis (EC), PEC merely requires a lower electrode potential to allow the separation of photogenerated e^- - h^+ pairs. The PEC technique not only overcomes the tough problem of effective powder catalyst recovery but also fully exploits the synergistic effect of light and electricity. A fundamental component of PEC cells is the semiconductor photoanode, which harvests solar energy and generates carriers. A perfect semiconductor photoanode should have favorable light absorption, a high redox potential, efficient charge transfer, and great water stability, all of which are critical factors. The key to developing PEC performance is to design and construct effective semiconductor photoanodes.

TiO$_2$-based photocatalysis has been the subject of a lot of interest in recent decades, owing to its non-toxicity, cost-effectiveness, and favorable electronic and photoelectrochemical properties[11,12]. In particular, highly ordered TiO$_2$ nanotube arrays TiO$_2$ (NTAs) with vertically grown tubular structures, large surface-to-volume ratios, extraordinary e^- - h^+ pairs separation capability, and excellent optoelectronic behavior are highly attractive[13–15]. These distinctive architectures allow for highly organized unidirectional electron transport pathways as well as more efficient active sites. However, TiO$_2$ NTAs still suffer from the inherent properties of large bandgap (Eg, 3.2 eV for anatase) and rapid e^- - h^+ recombination[16]. There is highly imperative to further exploit the decoration approaches of TiO$_2$ NTAs to obtain highly active PEC systems, thus promoting the implementation of TiO$_2$ NTAs in the utilization of solar energy.

Recent research has proposed step-scheme (S-scheme) heterojunctions, which are made up of two n-type semiconductors[17]. Compared with conventional heterojunctions, the S-scheme heterojunctions not only deliver effective separation of e^- - h^+ pairs motivated by an internal electric field (IEF) but also retain the highest redox capacity of photogenerated carriers. The reported Bi$_2$MoO$_6$/g-C$_3$N$_4$/Au S-scheme heterojunction is limited in its practical application by the requirement of loading noble metal Au[18]. Ma's group constructed Co$_3$O$_4$/C$_3$N$_4$ S-scheme heterojunctions for water purification in the PEC process, and the catalytic performance showed a significant reduction after five cycles of testing[19]. To construct noble metal-free and highly stable S-scheme heterojunctions for the efficient PEC degradation of SMT is therefore of great significance. Therefore, it is necessary to develop inexpensive and stable catalysts.

In recent years, Bi-based photocatalysts as a non-noble metal material exhibit some photocatalytic ability in the visible range due to the narrowing of the Eg by the hybridized VB of Bi 6 s and O 2p [20]. Considering the stability of Bi^{3+}, most researches have focused on compounds containing Bi^{3+}, such as (BiO)$_2$CO$_3$ [21], BiOX (X = Cl, Br, I) [22], BiVO$_4$ [23], Bi$_2$O$_3$ [24], Bi$_2$MO$_6$ (M = Mo, W) [25], and so on. The bismuth tin oxide (Bi$_2$Sn$_2$O$_7$), as a member of Bi-based photocatalysts, is recognized a desirable photocatalyst and is extensively used for the remediation of diverse environmental contaminants due to its unique pyrochlore structure, low cost, non-toxicity, high photosensitivity and suitable Eg (2.7 eV)[26]. In addition, it is a known fact that the catalytic performance of transition metal particles and supporting materials composites depends largely on the size, dispersion, and composition of the metal particles[27,28]. As a consequence, it is encouraging to design Bi$_2$Sn$_2$O$_7$ with quantum size so that it has tunable Eg and large intrinsic dipole moments for enhanced visible light response and fast charge separation[29]. Not only can Bi$_2$Sn$_2$O$_7$ quantum dots (QDs)

photosensitize TiO$_2$ NTAs, but the n-type characteristics and dramatically different work functions of Bi$_2$Sn$_2$O$_7$ QDs and TiO$_2$ NTAs predict that they are likely to form S-scheme Bi$_2$Sn$_2$O$_7$/TiO$_2$ NTAs heterojunction, allowing for the highest redox capacity. In photoelectrocatalytic systems, there are still problems of low light energy utilization, inefficient and unstable catalytic efficiency, and the microscopic mechanism of charge transfer in heterojunction catalysts under the simultaneous action of light and electricity has not been elucidated in detail.

In this work, a unique S-scheme heterojunction Bi$_2$Sn$_2$O$_7$/TiO$_2$ NTAs was fabricated by the hydrothermal process, which was the in-situ growth of Bi$_2$Sn$_2$O$_7$ QDs on TiO$_2$ NTAs, for PEC degradation of SMT. The Bi$_2$Sn$_2$O$_7$ QDs were uniformly dispersed on TiO$_2$ NTAs without obvious aggregation compared with pure Bi$_2$Sn$_2$O$_7$, thus maintaining the photoactive sites exposed on the surface while further extending the absorption range from the visible to near-infrared region. We explored the photoelectric properties of the prepared photoelectrodes, the effects of potential, pH, various foreign ions, and organic molecules on the PEC performance of Bi$_2$Sn$_2$O$_7$/TiO$_2$ NTAs heterojunction during SMT degradation, and the pathways of free radical generation. The existence of an IEF in the Bi$_2$Sn$_2$O$_7$/TiO$_2$ NTAs heterojunction can more efficiently separate photo-induced charge carriers, according to experimental tests and density functional theory (DFT) calculations. The formation of S-scheme charges transfer paths at the Bi$_2$Sn$_2$O$_7$/TiO$_2$ NTAs interface under the simultaneous action of light irradiation and external circuitry is discussed. The prepared Bi$_2$Sn$_2$O$_7$/TiO$_2$ NTAs photoelectrodes exhibited superior PEC degradation SMT activity and high stability under the irradiation of an LED lamp. This study provides an idea by the PEC process with S-scheme electron transfer driven catalysts for the efficient degradation of contaminants in water.

2. Experimental section

2.1. Photoelectrodes preparation

2.1.1. Preparation of TiO$_2$ NTAs

Scheme 1 illustrates the synthesis process. Organized self-assembled nanotubes of TiO$_2$ NTAs were obtained by electrochemical anodization of 2 × 3 cm^2 titanium foil (0.5 mm thickness, 99.99% purity) in 0.2 M H$_3$PO$_4$ + 0.3 M NH$_4$F aqueous solution [30]. The Ti foil was ultrasonically cleaned in acetone, anhydrous ethanol, and distilled water in that order before anodization. The above cleaned Ti foil was subjected to chemical polishing treatment in an aqueous solution with a volume ratio (HF: HNO$_3$: H$_2$O = 1:4:5) for 30 s, and then the surface was rinsed off with plenty of deionized water. The anodization was performed at room temperature with a Ti foil as the working electrode and a platinum foil as the counter electrode at 20 V for 30 min. The samples were promptly cleansed with deionized water and blown dry with N$_2$ after anodization. To convert the amorphous state to the crystalline state, the samples were heated in a muffle furnace at 500 °C for 2 h at a heating rate of 10 °C·min^{-1}. Ultimately, the target TiO$_2$ NTAs photoelectrodes were obtained.

2.1.2. Preparation of Bi$_2$Sn$_2$O$_7$/TiO$_2$ NTAs

All of the reagents were analytically pure and could be employed right away. In a typical reaction, Bi(NO$_3$)$_3$0.5 H$_2$O (1 mmol) was added to 15 mL of 2 mol·L^{-1} nitric acid solution. Na$_2$SnO$_3$ (1 mmol) was dissolved in 15 mL of deionized water and subsequently 0.36 g of hexadecyl trimethyl ammonium bromide (CTAB). The aforesaid two solutions were mixed and stirred for 30 min, and the pH was adjusted to 12 with 1 mol·L^{-1} NaOH during the stirring process. The mixture was equally divided into two parts and poured into two Teflon liners with a total capacity of 100 mL, wherein the TiO$_2$ NTAs photoanode was submerged and then sealed in the stainless steel autoclave and maintained at 180 °C for 24 h. Eventually, the pretreatment electrode was thoroughly rinsed with deionized water and ethanol and left to dry in the air
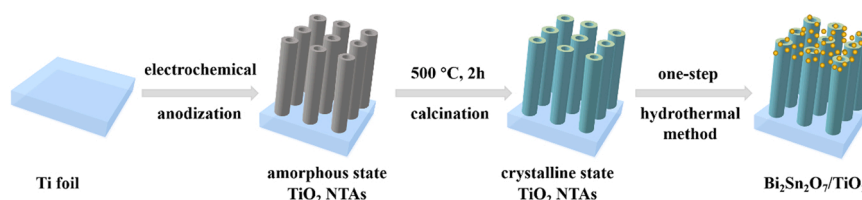
Scheme 1. Preparation of $Bi_2Sn_2O_7/TiO_2$ NTAs photoanodes.

to obtain $Bi_2Sn_2O_7/TiO_2$ NTAs photoelectrodes.

2.2. Characterization of the photoelectrodes

The powder x-ray diffraction (XRD, Ultima IV) using a diffractometer with Cu Kα radiation throughout the 2θ range of 20–80° was used to analyze the compositional phases of the obtained photoelectrodes. Field-emission scanning electron microscope (FE-SEM, LEO-1530VP), transmission electron microscopy (TEM, JEM-2800), and high-resolution TEM (HRTEM, JEM-2100 f) were used to determine the morphology and microstructure of the electrodes, and the compositions were examined by energy-dispersive spectroscopy (EDS) in the SEM. On a spectrometer (Thermo Scientific ESCALAB 250Xi) with a mono-chromatic Al-Kα X-ray Source, X-ray photoelectron spectra (XPS) were used to assess the element composition and surface valence variations of the electrode. The light absorption characteristics were detected using a UV–vis diffuse reflectance spectrophotometer (DRS, UV2600, Shimadzu, Japan) in the air against $BaSO_4$ in the region of 200–800 nm. Photoluminescence (PL) studies (F-2710, HITACHI, Japan) were conducted to investigate the optical properties of the samples. The electron paramagnetic resonance (EPR) measurements are performed using a spectrometer (Bruker EMX Nano, Germany) to detect the free-electron signal of samples in the PEC process. The total organic carbon (TOC) was used to estimate SMT mineralization using an Analytikjena multi N/C 3100 TOC analyzer.

2.3. Photoelectrochemical measurements

The photoelectrochemical measurements were performed using an electrochemical station (CHI 760E, China) with a standard three-electrode model. The prepared photoelectrodes were used as working electrodes, and the Pt foil and Ag/AgCl electrodes served as counter electrodes and reference electrodes, respectively. The electrolyte was Na_2SO_4 aqueous solution (0.1 M) and the photoanode was irradiated by a 50 W LED lamp (XC-50W1A5-OSP, China), with the light density parameter was 0.13 W/cm². The electrochemical impedance spectroscopy (EIS), linear sweep voltammogram (LSV), cyclic voltammetry curve (CV), and Mott-Schottky curves (MS) were all recorded using a CHI 760E electrochemical workstation. Photocurrent transient response curves and EIS were obtained on an applied potential of 1 V. At a frequency of 1000 Hz, the M-S curves were recorded. On an applied potential ranging from − 0.5–2.0 V, CV and LSV curves were measured.

2.4. The photoelectrocatalytic degradation experiments

To learn more about the catalytic performance, the prepared photoanode was employed as the anode and the Pt foil as the cathode in a quartz reaction cell (50 mL) with 0.1 M Na_2SO_4 as the electrolyte, the distance between the working electrode and counter electrode is about 1 cm, and 10 mg·L⁻¹ of SMT was degraded under the irradiation of an LED lamp (380 nm < λ < 840 nm). The photoanode is approximately 5 cm away from the light source. Under stirring circumstances, the effects of potential and pH on the catalytic performance of PEC were examined. The samples were collected at regular intervals during the degradation process and then filtered using a 0.45 μm PTFE filter.

2.5. Analytical methods

The concentration of SMT was determined using a high-performance liquid chromatography (HPLC) system (U3000, Thermo Fisher Scientific) with an AcclaimTM120 C18 column (3 μm, φ 3.0 × 100 mm) with a 270 nm DAD detector. At a flow rate of 0.5 mL min⁻¹, the mobile phase of acetonitrile: water was 7:13. The degradation pseudo-first-order kinetics of SMT was evaluated by the following Eq. (1)[31]:

$$-\ln\left(\frac{C_t}{C_0}\right) = kt \tag{1}$$

where C_0 (mg·L⁻¹) and C_t (mg·L⁻¹) are the concentrations of SMT at the initial and time t, respectively, and k is the first-order kinetic rate constant for the PEC process of SMT.

2.6. Determination of free radicals

Ammonium oxalate (AO), tert-Butanol (TBA), and furfuryl alcohol (FFA) serve as trapping reagents of h^+, $^•OH$, and $^1O_2$, respectively. To confirm the presence of $^•O_2^-$, nitro blue tetrazolium (NBT) was chosen as the scavenger of $^•O_2^-$ radical because NBT can be reduced by $^•O_2^-$ and form water-insoluble purple formazan[32]. This experiment was similar to the PEC degradation process of SMT, except that SMT was replaced by NBT. The change in NBT absorbance was detected by a spectrophotometer (752 N INESA, China) at 259 nm. The generated h^+ and ROS were determined with 100 mM 2, 2, 6, 6-tetramethylpiperidine 1-oxyl (TEMPO) and 100 mM 2,6-dimethylpyridine N-oxide (DMPO) by the electron paramagnetic resonance spectrometer (EPR, Bruker EMX Nano, Germany).

2.7. DFT calculations

First-principles calculations are implemented in the Vienna ab initio simulation package (VASP5.4.1) using the Perdew-Burke-Ernzerhof (PBE) method[33–35]. A planar wave cut-off energy of 400 eV was used within the framework of the projective augmented wave method. Integrating the Brillion region using the k-point set generated by Monkhorst-Pack found that a 3 × 3 × 1 k-point grid is sufficient for convergence calculations. All atoms were converged to 0.01 eV/A.

3. Results and discussion

3.1. Characterization of TiO_2 NTAs and $Bi_2Sn_2O_7/TiO_2$ NTAs photoelectrodes

The XRD measurements were performed to study the phase composition of these prepared samples. In Fig. 1a, the XRD patterns showed that the prepared $Bi_2Sn_2O_7$ QDs were in the cubic phase (JCPDS No. 88–0496). The diffraction peaks of TiO_2 NTAs were attributed to anatase TiO_2 (JCPDS No. 21–1272), rutile TiO_2 (JCPDS No. 21–1276), and Ti foil (JCPDS No. 41–1049), in which the major component was anatase [36]. For $Bi_2Sn_2O_7/TiO_2$ NTAs, apart from the characteristic reflections of TiO_2 NTAs, $Bi_2Sn_2O_7/TiO_2$ NTAs exhibited additional reflection at 28.8°, which was well-indexed to the (222) plane of $Bi_2Sn_2O_7$, confirming the formation of $Bi_2Sn_2O_7/TiO_2$ NTAs composites.
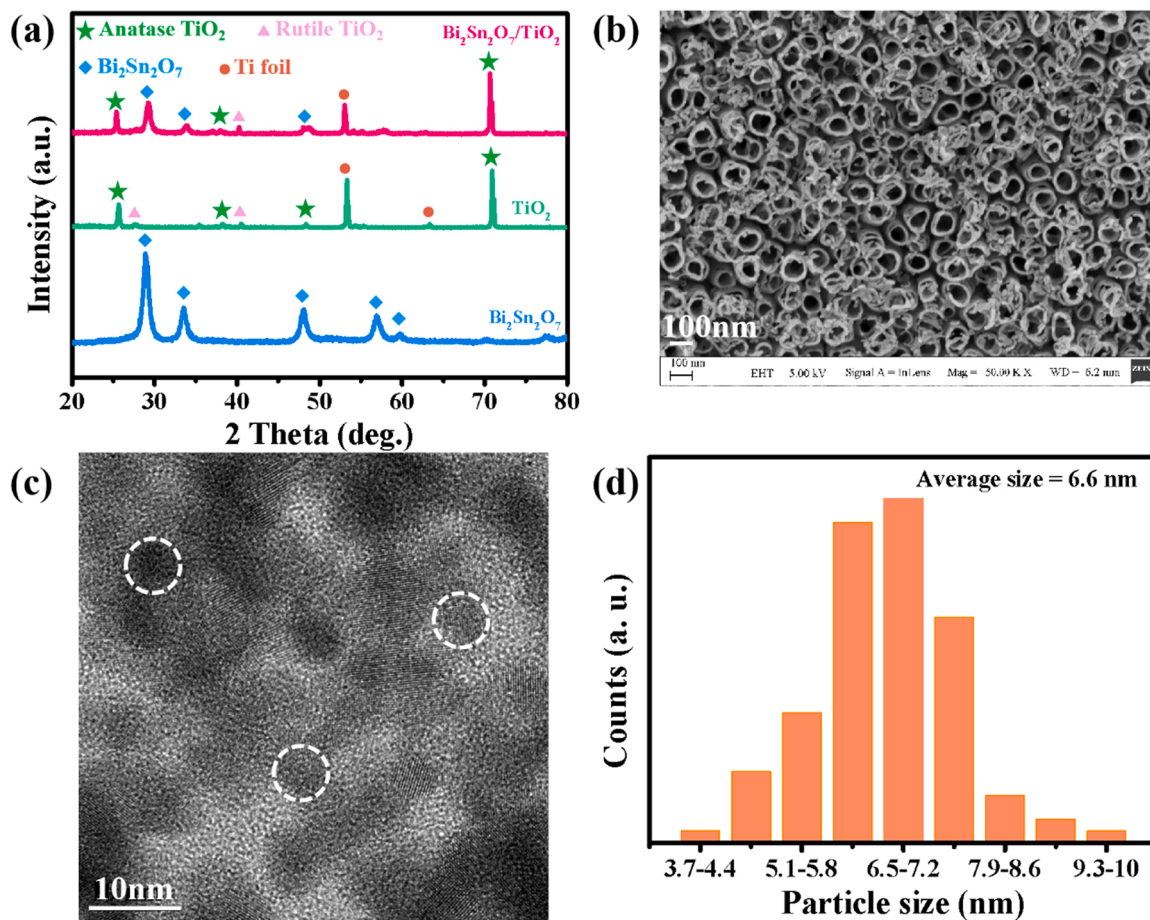
Fig. 1. XRD patterns (a) of $Bi_2Sn_2O_7$ QDs, TiO_2 NTAs, and $Bi_2Sn_2O_7/TiO_2$ NTAs; SEM image of (b) TiO_2 NTAs; TEM image (c) and size distribution (d) of the $Bi_2Sn_2O_7$ QDs.

Characterization of the microstructure and morphology of the photoelectrodes was carried out by SEM. As depicted in Fig. 1b, the tubular structure of TiO_2 NTAs was vertically oriented with top-end-open after anodic oxidation and calcination. The thickness and outer diameter were measured to be ~15 and ~110 nm, respectively, resulting in an inner diameter of approximately 80 nm. Fig. S1 shows the SEM image of $Bi_2Sn_2O_7$ QDs. As seen in Fig. 1c and d, the average size of the $Bi_2Sn_2O_7$ QDs is about 6.6 nm. Notably, numerous $Bi_2Sn_2O_7$ QDs were homogeneously attached to the TiO_2 NTAs surface, which provided a great opportunity for carrier migration (Fig. 2a). The morphology of $Bi_2Sn_2O_7/$ TiO_2 NTAs composites was further explored by TEM and HRTEM. Fig. 2b shows that $Bi_2Sn_2O_7$ QDs (marked by white circles) form a tight
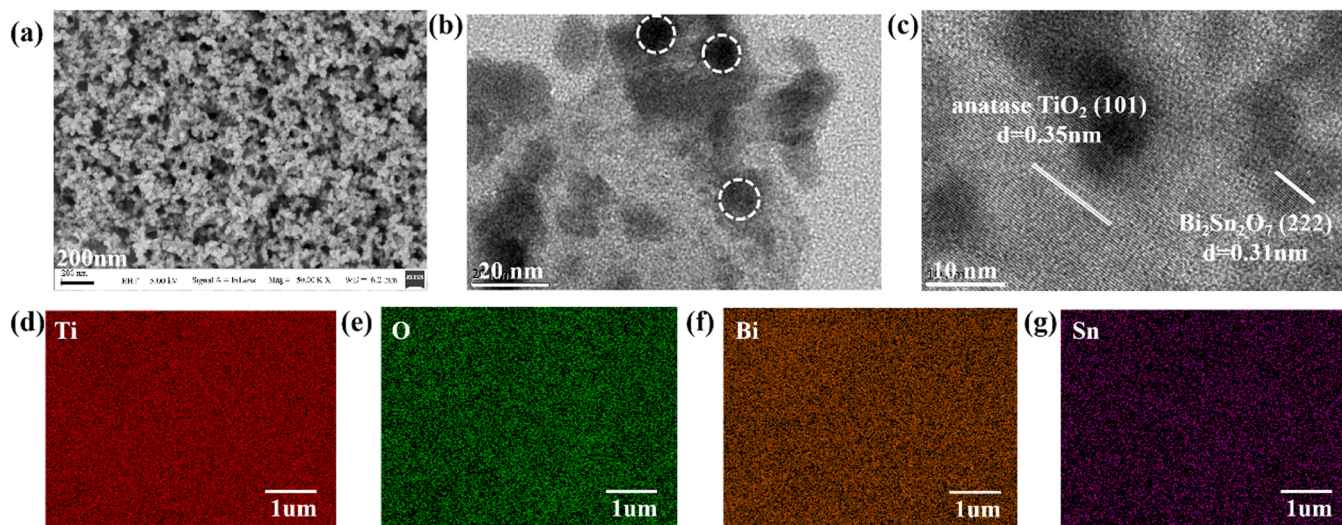

Fig. 2. SEM image of (a) $Bi_2Sn_2O_7/TiO_2$ NTAs; HRTEM images (b, c) $Bi_2Sn_2O_7/TiO_2$ NTAs; the corresponding EDS elemental mapping (d-g) images of $Bi_2Sn_2O_7/$ TiO_2 NTAs.

interface with the TiO$_2$ NTAs, which facilitates the charge transfer between the two components. As shown in Fig. 2c, the lattice spacings of 0.35 and 0.31 nm corresponded to the anatase TiO$_2$ (101) plane and the cubic Bi$_2$Sn$_2$O$_7$ (222) plane, respectively. From the EDS elemental mapping presented in Fig. 2d-g, the elements Ti, O, Bi, and Sn were evenly scattered across the selected region (Fig. S2), demonstrating the successful complex of Bi$_2$Sn$_2$O$_7$ QDs and TiO$_2$ NTAs.

The surface structure was further investigated by XPS measurements. The XPS survey scan (Fig. 3a) could reveal all elements of TiO$_2$ NTAs and Bi$_2$Sn$_2$O$_7$ QDs in the composites, a further indication of their ready complexity. In the O 1 s, XPS spectra (Fig. 3b) of Bi$_2$Sn$_2$O$_7$/TiO$_2$ NTAs, the binding energy of lattice oxygen atoms and surface oxygen were 529.42 and 531.07 eV, respectively. The positions of oxygen-containing species at TiO$_2$ and Bi$_2$Sn$_2$O$_7$ moved toward low and high binding energy, respectively, illustrating the gain and loss of electrons due to electronic interactions in the composites. There were two main peaks yielded with Bi 4 f XPS spectra (Fig. 3c) of Bi$_2$Sn$_2$O$_7$/TiO$_2$ NTAs, which ascribed to the 4 f$_{5/2}$ (164.24 eV) and 4 f$_{7/2}$ (158.88 eV) binding energy of Bi^{3+}, respectively [37]. Fig. S3 showed that Sn 3d$_{3/2}$ and Sn 3d$_{5/2}$ in Bi$_2$Sn$_2$O$_7$ corresponded to 494.02 and 485.60 eV, respectively [38]. The Ti 2p XPS spectra (Fig. 3d) of Bi$_2$Sn$_2$O$_7$/TiO$_2$ NTAs showed symmetrical Ti 2p doublets of Ti^{4+} ions [39]. It is well observed from the ex-situ XPS spectra that after the combining of TiO$_2$ NTAs and Bi$_2$Sn$_2$O$_7$ QDs, the binding energy of Bi 4 f, Sn 3d, and O 1 s in Bi$_2$Sn$_2$O$_7$ could shift to a higher direction, while Ti 2p and O 1 s in TiO$_2$ turn to a lower direction, demonstrating a change in the local chemical environment of the surface elements [40]. These above shifts suggest that electrons are transferred from Bi$_2$Sn$_2$O$_7$ to TiO$_2$ after hybridization because of the different work functions of the two semiconductors [41]. This electron transfer creates an internal electric field (IEF) at the interface between TiO$_2$ NTAs and

Bi$_2$Sn$_2$O$_7$ QDs, which facilitates the construction of S-scheme Bi$_2$Sn$_2$O$_7$/TiO$_2$ NTAs heterojunctions, allowing effective charge carriers separation and thus promoting the PEC degradation of SMT. In addition, in-situ irradiation XPS measurements of Bi$_2$Sn$_2$O$_7$/TiO$_2$ NTAs showed that the binding energy of Ti 2p and O 1 s in Bi$_2$Sn$_2$O$_7$/TiO$_2$ NTAs composites under light irradiation moved significantly to higher energy levels compared with those in the dark environment, while the binding energy of Bi 4 f and Sn 3d in the nanocomposites significantly moved to lower energy levels, indicating the transfer of photogenerated electrons from TiO$_2$ to Bi$_2$Sn$_2$O$_7$ under illumination. The binding energy of O 1 s was shifted to higher energy levels since more of the oxygen species originate from TiO$_2$, as can be seen in Table S1. Therefore, these XPS results provide crucial evidence for the carrier transfer pathway at the Bi$_2$Sn$_2$O$_7$/TiO$_2$ NTAs heterojunction interface under light irradiation. Among them, the migration of photogenerated electrons from TiO$_2$ to Bi$_2$Sn$_2$O$_7$ is in good agreement with the S-scheme mechanism.

In the exploration of electron transfer in semiconductor heterojunction, the work function (Φ) is also an important metric. It can be determined from the energy difference of the electrostatic potential of the material from the vacuum energy level and the Fermi energy level. Fig. 4a and b reveal that the work function of TiO$_2$ (101) and Bi$_2$Sn$_2$O$_7$ (222) was 6.24 and 4.99 eV, respectively, signifying that the Fermi level of TiO$_2$ was lower than that of Bi$_2$Sn$_2$O$_7$[41]. When TiO$_2$ and Bi$_2$Sn$_2$O$_7$ come into contact, the electrons of Bi$_2$Sn$_2$O$_7$ will flow to TiO$_2$, driving the two phases to be at the same Fermi level and creating IEF at the Bi$_2$Sn$_2$O$_7$/TiO$_2$ NTAs interface. Such results are in full agreement with the XPS results, which are favorable for promoting charge separation and improving the PEC activity of SMT.

The optical absorption properties of the prepared photoanodes were studied using UV–vis DRS. The absorption edges of pristine TiO$_2$ NTAs,
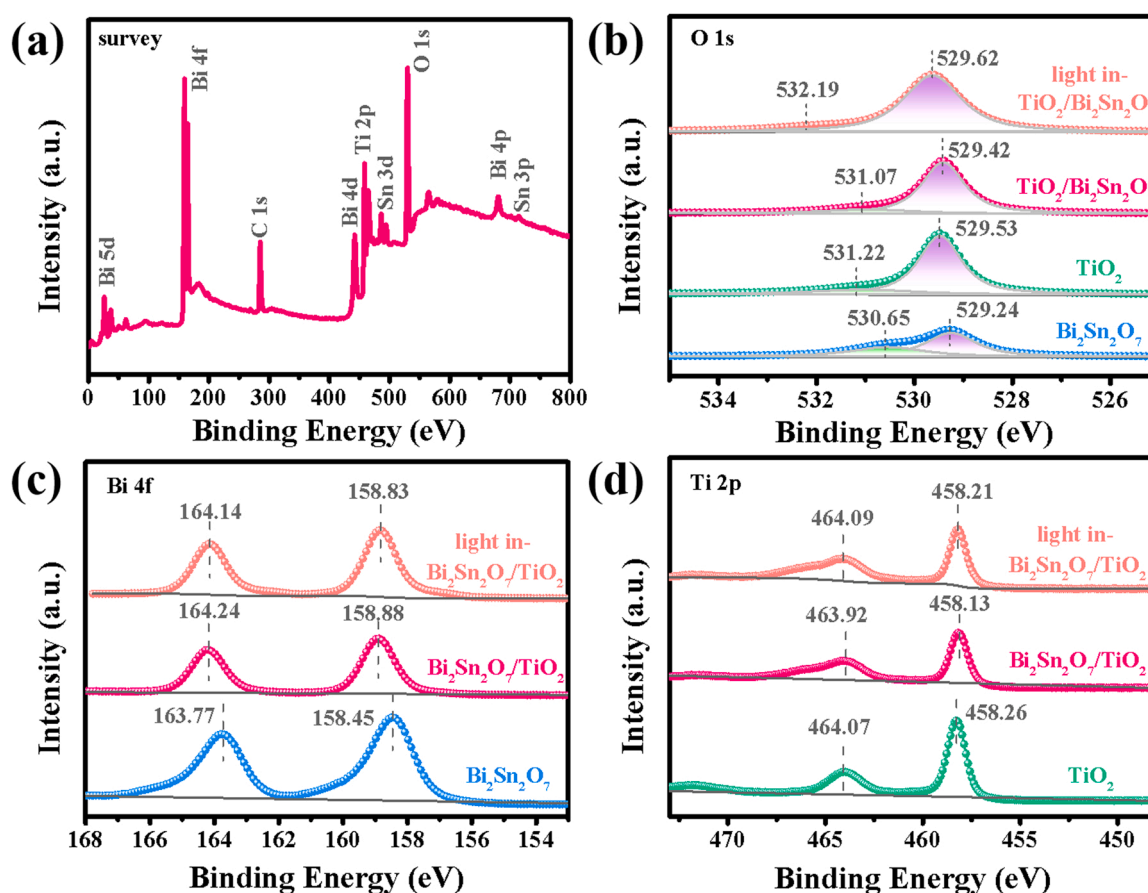

Fig. 3. In-situ and ex-situ XPS spectra of survey (a), O 1 s (b), Bi 4 f (c), and Ti 2p (d) of Bi$_2$Sn$_2$O$_7$ QDs, TiO$_2$ NTAs, and Bi$_2$Sn$_2$O$_7$/TiO$_2$ NTAs. In-situ XPS spectra were collected under light irradiation.
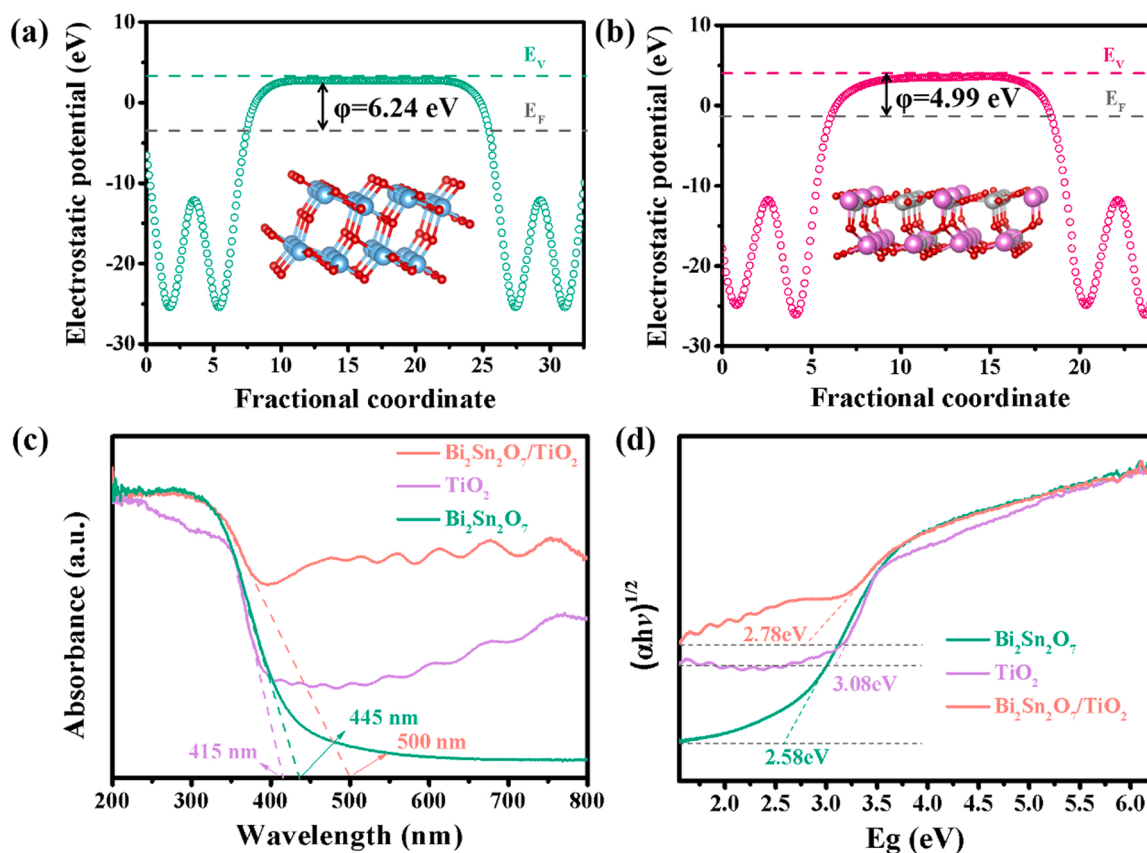
Fig. 4. The electrostatic potentials of (a) anatase TiO_2 (101), (b) $Bi_2Sn_2O_7$ (222) facets. The red, blue, gray, and purple spheres stand for O, Ti, Sn, and Bi atoms, respectively. Gray and green (red) dashed lines indicate the vacuum and Fermi energy levels; UV–vis DRS (c); the Eg of TiO_2 NTAs, $Bi_2Sn_2O_7$ QDs, and $Bi_2Sn_2O_7/TiO_2$ NTAs samples (d).

$Bi_2Sn_2O_7$ QDs, and $Bi_2Sn_2O_7/TiO_2$ NTAs were located at 415, 445, and 500 nm (Fig. 4c), corresponding to the Eg of 3.08, 2.58, and 2.78 eV (Fig. 4d), respectively. The value of VB in TiO_2 NTAs and $Bi_2Sn_2O_7$ QDs are 2.39 and 1.03 eV, respectively, as shown in Fig. S4, and it can be derived from Eq. (2) that the value of CB in TiO_2 and $Bi_2Sn_2O_7$ are -0.69 and -1.55 eV, respectively [42]. In comparison with pristine TiO_2 NTAs, the composite $Bi_2Sn_2O_7/TiO_2$ NTAs had a significant redshift due to the modification of $Bi_2Sn_2O_7$ QDs, with the absorption band edge at 500 nm and exhibited higher absorption at $400 \sim 800$ nm. The $Bi_2Sn_2O_7/TiO_2$ NTAs heterojunction has good light absorption ability, especially in the absorption range from visible to near-infrared region, which is expected to improve PEC performance. The photoluminescence (PL) intensity in photocatalysis is directly related to the separation efficiency of $e^- - h^+$ pairs. It could be seen from Fig. S5 that $Bi_2Sn_2O_7/TiO_2$ NTAs had a lower PL intensity compared with pristine TiO_2, indicating that $e^- - h^+$ pairs were greatly suppressed for recombination and the separation and transport were more efficient.

$$E_{CB} = E_{VB} - E_g \qquad (2)$$

A series of photoelectrochemical measurements were employed to identify the effect of the photoelectric characteristics of $Bi_2Sn_2O_7/TiO_2$ NTAs hybrids. The EIS measurements provided insights into the charge transfer behavior of the photoelectrodes interface. In general, the smaller the radius of the arc in the EIS Nyquist plots, the lower the corresponding charge transfer resistance (R_{ct}) and the faster the process of interfacial carrier transfer. Under LED lamp illumination, Fig. 5a presented typical EIS Nyquist plots of $Bi_2Sn_2O_7/TiO_2$ NTAs and TiO_2 NTAs photoelectrodes. The Rct of the $Bi_2Sn_2O_7/TiO_2$ NTAs photoelectrode (26.4 Ω) was much reduced compared to TiO_2 (627.1 Ω), which meant that $Bi_2Sn_2O_7/TiO_2$ NTAs had more efficient charge

migration and better conductivity, and the equivalent circuit models were shown in Fig. S6. Owing mainly to the formation of an IEF in the $Bi_2Sn_2O_7/TiO_2$ NTAs heterojunction, which dramatically boosted the charge separation efficiency and charge transport capacity at the interface. To evaluate the separation and transfer of photogenerated carriers, the transient photocurrent response of TiO_2 NTAs and $Bi_2Sn_2O_7/TiO_2$ NTAs heterojunction photoanodes were characterized. As demonstrated in Fig. 5b, the photocurrent density of the photoanode varied in a well-correlated manner with the on/off cycle. The photocurrent density of $Bi_2Sn_2O_7/TiO_2$ NTAs was 68.7 uA·cm^{-2}, which was about twice as much as that of TiO_2 NTAs (34.5 uA·cm^{-2}), suggesting that $Bi_2Sn_2O_7/TiO_2$ NTAs had more electrons flowing from the anode to the cathode. The formation of S-scheme heterojunction in the $Bi_2Sn_2O_7/TiO_2$ NTAs hybrid suppressed the recombination of photogenerated $e^- - h^+$ pairs, yielding a scaled-up photocurrent. The higher photocurrent response favored the PEC efficiency, which was confirmed by the increased photocurrent of $Bi_2Sn_2O_7/TiO_2$ NTAs in the region of -0.5–2.0 V in the LSV diagram (Fig. 5c). The $Bi_2Sn_2O_7/TiO_2$ NTAs photoanode generates photogenerated $e^- - h^+$ under light illumination, and the e^- are transferred to the counter electrode by an external circuit, which causes a change in the current. The current density of the $Bi_2Sn_2O_7/TiO_2$ NTAs hybrid photoanode was 38.5 uA·cm^{-2} when the potential was 2.0 V, which was 1.7 times greater than that of pure TiO_2 NTAs (22.6 uA·cm^{-2}). The increase in current density was attributed to the $Bi_2Sn_2O_7/TiO_2$ NTAs composites that suppressed the recombination of photogenerated $e^- - h^+$ pairs, thus more e^- and h^+ were involved in the generation of free radicals, and the generated more free radicals promoted the photoelectrocatalytic degradation activity of SMT. In particular, the onset potential of the $Bi_2Sn_2O_7/TiO_2$ NTAs heterojunction was negatively shifted concerning that of TiO_2 NTAs (Fig. 5c inset),
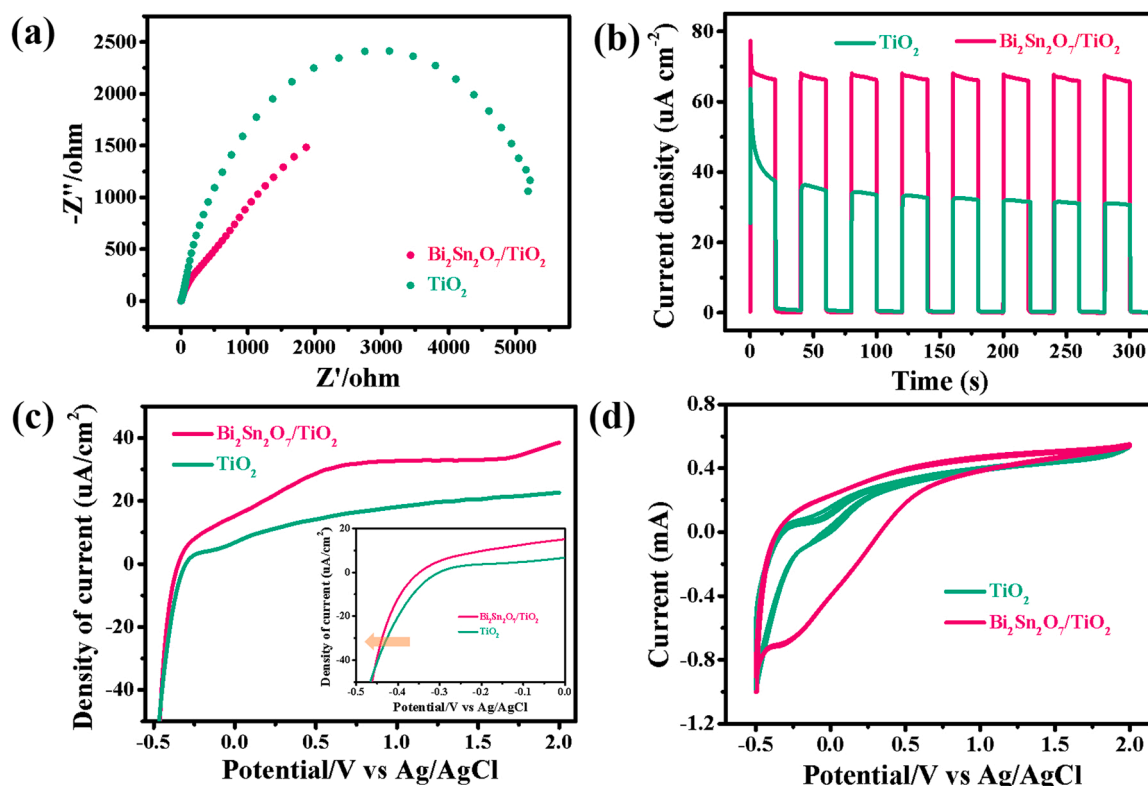
Fig. 5. (a) EIS Nyquist plots; (b) Photocurrent transient response curves; (c) Linear sweep voltammograms, the inset in (c) shows the difference in onset potential; (d) Cyclic voltammetry curves of the as-prepared photoelectrodes in 0.1 M Na$_2$SO$_4$.

reflecting a smaller charge transfer kinetic energy barrier through the TiO$_2$ NTAs and Bi$_2$Sn$_2$O$_7$ QDs interface. The CV curves (Fig. 5d) were employed to estimate the active area of the PEC, which were recorded for TiO$_2$ NTAs and Bi$_2$Sn$_2$O$_7$/TiO$_2$ NTAs photoelectrodes in the potential within − 0.5–2 V. As expected, the confined area of Bi$_2$Sn$_2$O$_7$/TiO$_2$ NTAs photoelectrode was substantially larger than that of TiO$_2$ NTAs, reflecting its outstanding PEC performance. To investigate the type of TiO$_2$ and Bi$_2$Sn$_2$O$_7$, the M-S plots were further measured. As displayed in Fig. S7, the slope of the linear part of the two curves is positive in the M-S curves, implying that both TiO$_2$ and Bi$_2$Sn$_2$O$_7$ are n-type semiconductors, which are compatible with the type of formation of S-scheme heterojunctions[43].

3.2. SMT photoelectrocatalytic degradation activity of Bi$_2$Sn$_2$O$_7$/TiO$_2$ NTAs composites

In this work, the PEC performance of the photoelectrodes was assessed by PEC degradation of SMT in 0.1 M Na$_2$SO$_4$ electrolyte at a potential of 1 V for 120 min. As demonstrated in Fig. 6a, the corresponding removal efficiency of TiO$_2$ NTAs and Bi$_2$Sn$_2$O$_7$/TiO$_2$ NTAs is 63.9% and 90.3%, respectively. In contrast to pure TiO$_2$ NTAs, the Bi$_2$Sn$_2$O$_7$/TiO$_2$ NTAs heterojunction showed a pronounced advantage in the PEC degradation of SMT. This enhancement comes from the increased efficiency of light-harvesting and carrier separation due to the S-scheme heterojunction. The plots of -ln (C$_t$/C$_0$) versus t were found to be a linear relationship after curve fitting (Fig. 6b), and the degradation of SMT matched pseudo-first-order kinetics. The pseudo-first-order rate constant of Bi$_2$Sn$_2$O$_7$/TiO$_2$ NTAs composites ($k = 0.0189$ min^{-1}) was 2.6 times higher than that of TiO$_2$ NTAs ($k = 0.0074$ min^{-1}). The TOC removal of SMT at 2 h was about 57.8% (Fig. S8).

The Bi$_2$Sn$_2$O$_7$/TiO$_2$ NTAs photoelectrode was examined in both PC and EC conditions. Fig. 6c and d demonstrate that the degradation efficiency in the PC process after 120 min of SMT reaction was only 16.6%, and there was almost no catalytic performance in the EC process

at 1 V. Excitingly, the PEC process achieves a removal efficiency of 90.3%, which is almost 5 times higher than the sum of the first two processes. As a result, in the PEC process, a synergistic effect can be expected, and the synergistic factor (SF) can be determined using Eq. (3), yielding a calculated SF of 10.1[44].

$$SF = \frac{k_{PEC}}{k_{EC} + k_{PC}} - 1 \tag{3}$$

where k_{PEC}, k_{EC}, and k_{PC} denote the degradation rate constants of SMT in PEC, PC, and EC processes, respectively. The values of k_{PEC}, k_{EC}, and k_{PC} in this work are 0.0189, 0.0003, and 0.0014 min^{-1}, respectively.

The applied potential plays an essential role in the photogenerated charge separation and transport during the PEC process, which ultimately enhances the degradation efficiency. To investigate the degrading performance in a 10 mg·L^{-1} SMT simulated wastewater system, a range of applied potential was chosen (Fig. 7a and b). In the region of 0 ∼ 1.0 V, the degradation rate increased in a potential-dependent manner, and the removal rate peaked when the potential reached 1.0 V because of the easy and sufficient separation of photogenerated carriers. Nevertheless, when the potential exceeded 1.0 V, the response efficiency hardly improved anymore. The extent of the electrochemical enhancement (E, %) was evaluated by the subsequent Eq. (4):

$$E = \frac{k_{PEC} - k_{PC}}{k_{PEC}} \times 100\% \tag{4}$$

The corresponding k_{PEC} values are 0.0087, 0.0140, 0.0189, 0.0194, 0.0202 min^{-1} when the potential is 0.2, 0.5, 1.0, 1.5, 2.0 V respectively. The E values were 83.9% and 90.0% when the potential was 0.2 and 0.5 V, respectively, and their corresponding PEC degradation efficiency was 68.2% and 82.8%, respectively. Notably, the E value increased to 92.5% when the potential was 1.0 V. The trend of enhancement slowed down when the potential was varied to 1.5 and 2.0 V, where the E values increased to 92.8% and 93.1%, respectively, and there is no obvious
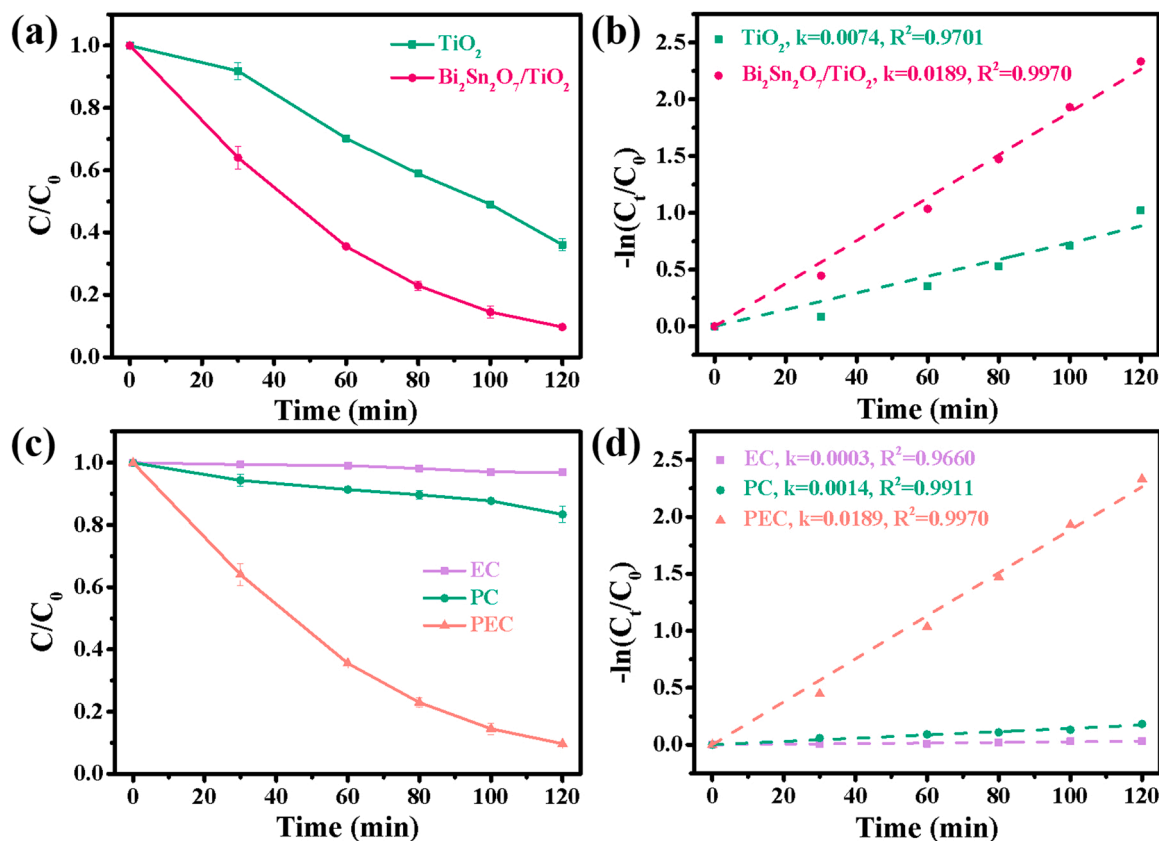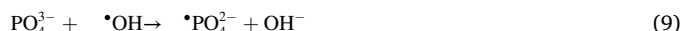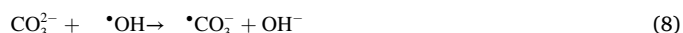
Fig. 6. The PEC degradation rate (a), pseudo-first-order kinetic curves (b) of SMT by TiO$_2$ NTAs and Bi$_2$Sn$_2$O$_7$/TiO$_2$ NTAs photoelectrodes; (c) comparison of SMT degradation rate and (d) pseudo-first-order kinetic curves using Bi$_2$Sn$_2$O$_7$/TiO$_2$ NTAs photoelectrode under different processes (PEC, PC, and EC). Experimental conditions: initial SMT concentration = 10 mg·L^{-1}, Na$_2$SO$_4$ concentration = 0.1 M, pH = 5.7.

improvement in degradation efficiency. In an attempt to provide cost-effective recommendations in a real water environment, 1.0 V is therefore chosen as the energy-conservation operating potential.

The initial pH of the solution is one of the vital factors affecting the removal rate of SMT and has a substantial impact on the surface charge and oxidation potential of the photoelectrode, so we performed the measurements in a wide pH range of 3–11. When the pH varied from 3 to 5.7 (natural pH of 10 mg·L^{-1} SMT in 0.1 M Na$_2$SO$_4$), the degradation efficiency steadily improved, as seen in Fig. 7c, and the degradation efficiency of PEC becomes worse instead with a further increase in pH. The degradation efficiency of SMT was maximum when in a weak acid (pH=5.7) condition with the largest rate constant (Fig. 7d), which can be explained by the following reasons: (i) The nature of the target pollutant. SMT has an amino group, which has alkaline properties in wastewater and therefore is conducive to the degradation of pollutants in an acidic environment. (ii) The oxidation capacity of photoanode. The VB of the photoanode shifts to a more negative potential as the pH increases, thus limiting the e$^-$ - h$^+$ separation when the pH increases, leading to a reduction in the oxidation capacity of the catalyst. (iii) The change in redox potential. The redox potential of SMT decreases when the pH increases. SMT can directly absorb some of the photogenerated e$^-$ generated under the photoelectric effect, so the thermodynamic driving force decreases when the pH increases [36,45,46]. As such, an optimal pH value exists under acidic conditions to achieve efficient degradation of SMT by the PEC process.

The co-existing anions and humic acids (HA) in wastewater purification usually affect the degradation efficiency of the catalytic system. PEC degradation of SMT by composites was carried out under optimal operating conditions by incorporating 10 mM of Cl$^-$, CO$_3^{2-}$, PO$_4^{3-}$ and, 10 mg·L^{-1} of HA, respectively. As can be seen in Fig. 7e, all of the incorporations subjected SMT degradation to varying degrees of

retardation. The decline caused by HA is due to its degradability, which will compete with SMT for free radicals, leading to a loss of degradation efficiency of SMT [47]. As for Cl$^-$, it can react with $^{\bullet}$OH and h$^+$ (Eqs. (5)–(7)), leading to a modest decrease in the degradation of SMT [48]. The conversion of CO$_3^{2-}$ and PO$_4^{3-}$ to the weaker selective radicals CO$_3^{2-}$ and PO$_4^{3-}$ by consuming $^{\bullet}$OH can be seen from Eqs. (8) and (9), respectively [36]. Fig. 7f showed that the order of effect of the co-existing anions was PO$_4^{3-}$ > CO$_3^{2-}$ > Cl$^-$. The order of this discrepancy is because $^{\bullet}$Cl is more oxidizing than $^{\bullet}$PO$_4^{2-}$ and $^{\bullet}$CO$_3$, and the more negatively charged the anion, the stronger its electrostatic attraction[49].

$$Cl^- + \ ^{\bullet}OH \rightarrow \ ^{\bullet}HOCl^- \tag{5}$$

$$^{\bullet}HOCl^- + H^+ \rightarrow \ ^{\bullet}Cl + \ H_2O \tag{6}$$

$$Cl^- + h^+ \rightarrow \ ^{\bullet}Cl \tag{7}$$

$$CO_3^{2-} + \ ^{\bullet}OH \rightarrow \ ^{\bullet}CO_3^- + OH^- \tag{8}$$

$$PO_4^{3-} + \ ^{\bullet}OH \rightarrow \ ^{\bullet}PO_4^{2-} + OH^- \tag{9}$$

Furthermore, our results outlined in Table 1 for comparison with other reported similar systems of PEC degradation of organic compounds, from which we can see that the degradation efficiency of the prepared Bi$_2$Sn$_2$O$_7$/TiO$_2$ NTAs photoelectrodes reached more than 90% at 2 h, even when we work with a non-expensive and environmentally friendly 50 W LED lamp.

3.3. Photoelectrocatalytic mechanism of S-scheme Bi$_2$Sn$_2$O$_7$/TiO$_2$ NTAs heterojunction

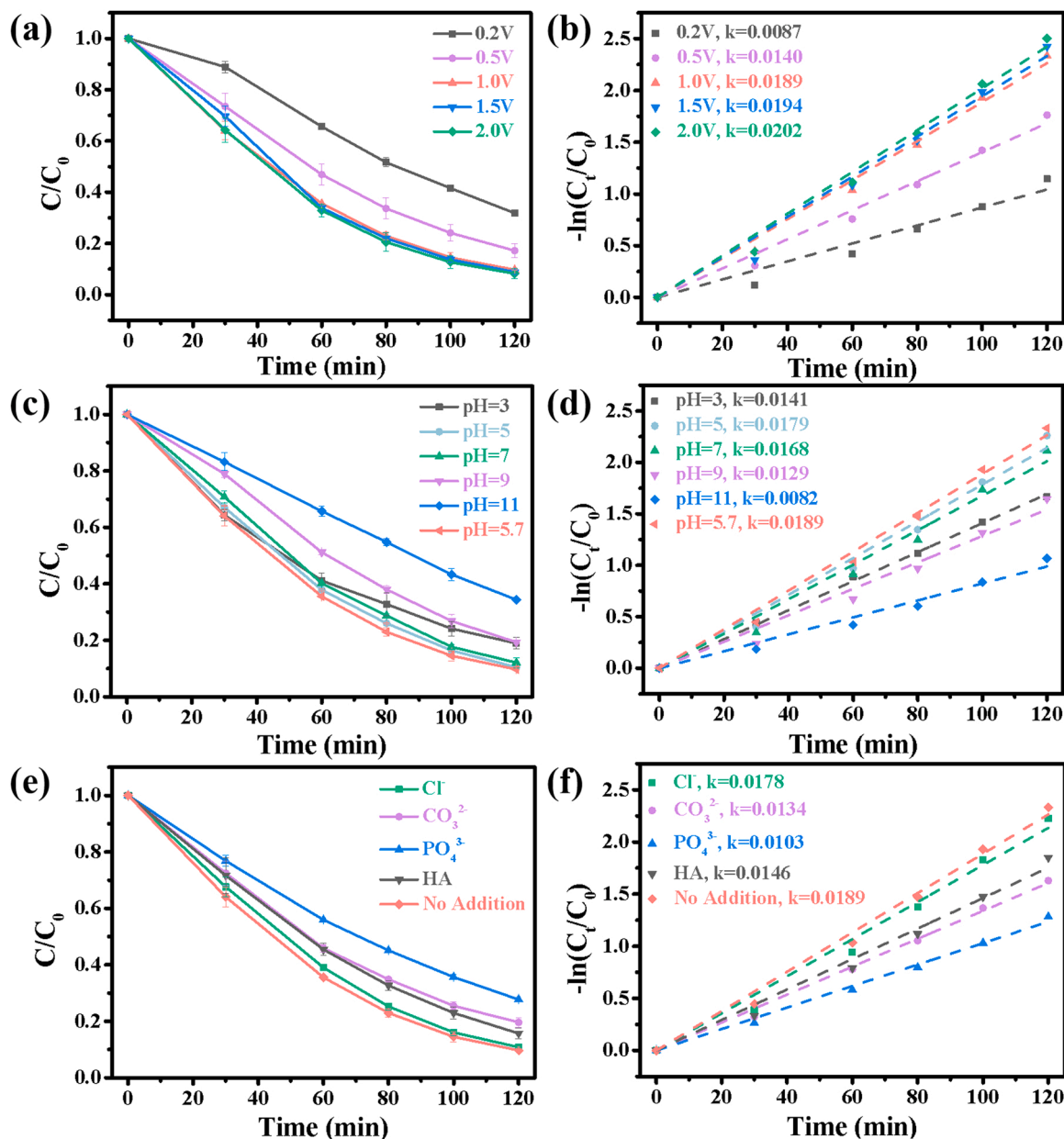Free radical quenching investigations on the key active substances

Fig. 7. The effect of operational parameters on PEC degradation SMT of over $Bi_2Sn_2O_7/TiO_2$ NTAs photoelectrode within 120 min: (a) effect of external potential and pseudo-first-order kinetic curves (b); (c) effect of initial pH and pseudo-first-order kinetic curves (d); (e) effect of co-existing anions and pseudo-first-order kinetic curves (f).

were done employing a range of scavenges in an attempt to uncover the main reactive species of SMT degradation. As shown in Fig. 8a, the concentration of AO varied from 0 to 50 mM, and the removal efficiency of SMT decreased from 90.3% to 74.3%, which was a significant reduction of 16%. In the case of scavenging for $^\bullet OH$, the degradation rate of SMT decreases only slightly by 9.7% in Fig. 8b, suggesting that the contribution of $^\bullet OH$ could not be neglected. As the FFA dosing was increased, the degradation of SMT was apparently inhibited to 51.9% (Fig. 8c), implying that the non-radical pathway ($^1O_2$) is also a crucial ROS in the degradation of SMT. Fig. 8d showed the evolution of NBT disappearance during the PEC process over $Bi_2Sn_2O_7/TiO_2$ NTAs photoanode. Both 5 and 10 $mg \cdot L^{-1}$ of NBT were reduced under the PEC process and insoluble purple formazan was observed on the counter electrode Pt foil, indicating the presence of $^\bullet O_2^-$. This is due to the migration of photogenerated e^- to the counter electrode in response to external potential and the reduction of O_2 in a single-electron process to

produce $^\bullet O_2^-$. In the two-electron process, O_2 is reduced to form H_2O_2 (Fig. S9). Thus, h^+, $^\bullet O_2^-$ and, $^1O_2$ are the major effective active species for SMT degradation, with $^\bullet OH$ also playing an auxiliary role.

The results of the capture experiments were further verified with ESR. Fig. 9a and b showed the ESR signals of DMPO-$^1O_2$ and TEMPO-h^+. For the case of $^1O_2$, the intensity was upgraded under the photoelectric effect, indicating the production of $^1O_2$. The h^+ sacrificial agent of $Bi_2Sn_2O_7/TiO_2$ NTAs was depleted, confirming the existence of photogenerated h^+ in the $Bi_2Sn_2O_7/TiO_2$ NTAs system. The outcomes of EPR are consistent with the conclusions of the capture experiments, according to the preceding analysis.

For the purpose of evaluating the stability of the prepared photoelectrode, cyclic degradation experiments of SMT were conducted. As seen in Fig. 9c, the performance of $Bi_2Sn_2O_7/TiO_2$ NTAs did not show any significant decline, and more than 90% of SMT was still removed after five consecutive cycles. Besides, the great stability of the $Bi_2Sn_2O_7/$

Table 1

The comparison of PEC degradation performance for organic pollutants between $Bi_2Sn_2O_7/TiO_2$ NTAs photoelectrode and other reported photoelectrocatalysts.

Working electrode	Counter electrode	Pollutant	Light source	Removal efficiency	Condition	Ref.
ZIF-8/NF-TiO$_2$	Cu sheet	SMT (10 mg/L)	300 W Xe lamp ($\lambda > 420$ nm)	81.3% (3 h) $k = 0.0091$ min^{-1}	0.5 M Na$_2$SO$_4$; external potential= 2.0 V pH= 3.5	[36]
graphite/TiO$_2$	Pt	Methyl orange (10 mg/L)	500 W Xe lamp ($\lambda > 420$ nm)	99% (2 h) $k = 0.0244$ min^{-1}	0.1 M Na$_2$SO$_4$; external potential= 2.0 V	[50]
TiO$_2$/Ti	Pt	Dimethyl phthalate (2 mg/L)	300 W Xe lamp (320 nm $< \lambda <$ 780 nm)	99% (1 h) $k = 0.0794$ min^{-1}	0.1 M Na$_2$SO$_4$; external potential= 0.6 V pH= 7	[51]
g-C$_3$N$_4$/TiO$_2$ NTAs	Pt	Phenol (5 mg/L)	500 W Xe lamp	99% (2.5 h)	1 mM Na$_2$SO$_4$ external potential= 1.0 V	[52]
Ag/AgCl/TiO$_2$-NTs	Pt	microcystin-LR (1 mg/L)	60 W incandescent lamps ($\lambda > 400$ nm)	99% (6 h) $k = 0.0082$ min^{-1}	0.01 M NaNO$_3$ external potential= 0.6 V	[53]
Blue-TiO$_2$ NTAs	stainless steel	4-chlorophenol (100 μM)	300-W Xe arc lamp ($\lambda > 320$ nm)	99% (2 h)	0.1 M Na$_2$SO$_4$ external potential= 1.11 V	[54]
Bi$_2$Sn$_2$O$_7$/TiO$_2$ NTAs	Pt	SMT (10 mg/L)	50 W LED lamp (380 nm $< \lambda <$ 840 nm)	90% (2 h) $k = 0.0189$ min^{-1}	0.1 M Na$_2$SO$_4$ external potential= 1.0 V pH= 5.7	This work
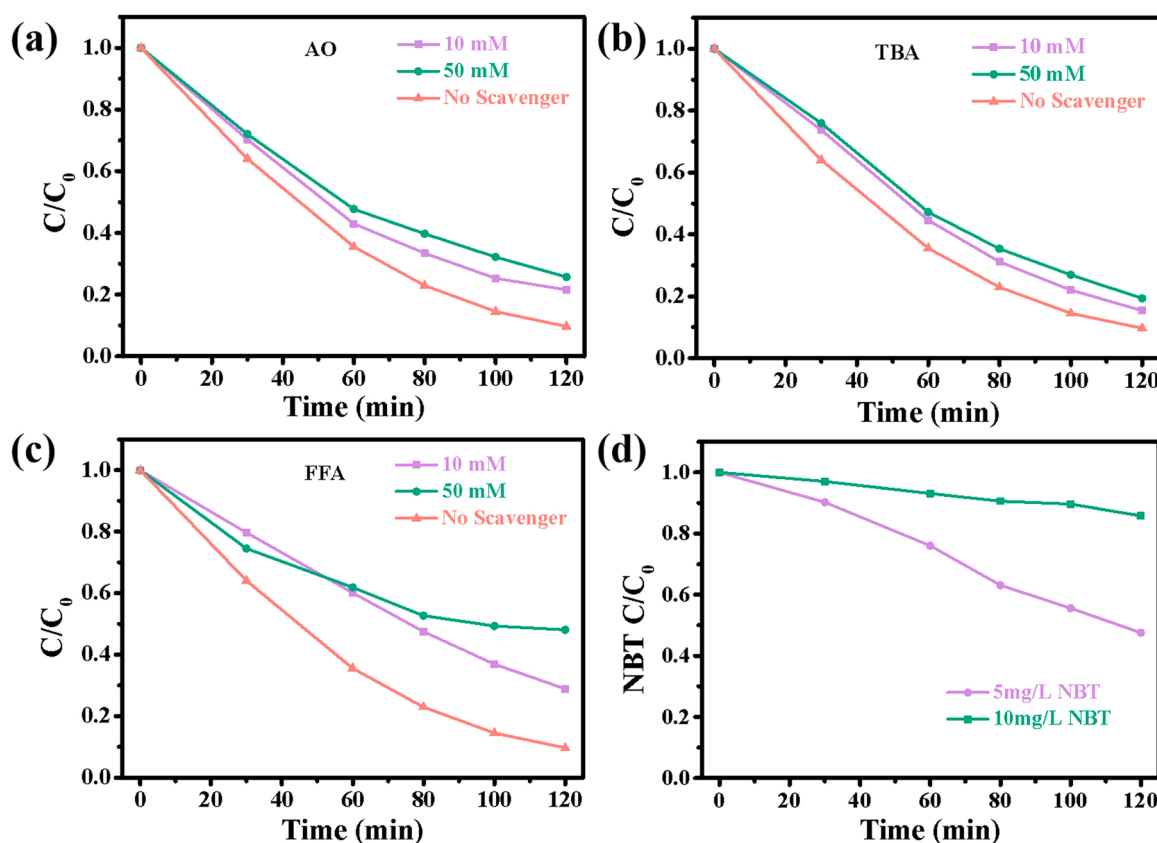
Fig. 8. The quenching experiments used AO for h^+ (a), TBA for $^•OH$ (b), and FFA for $^1O_2$ (c). The NBT decomposition during the PEC over $Bi_2Sn_2O_7/TiO_2$ NTAs and TiO_2 for detecting $^•O_2^-$ (d).

TiO_2 NTAs photoelectrode was further supported by XRD. It is noteworthy that the phase structure of $Bi_2Sn_2O_7/TiO_2$ NTAs after use is almost identical to that of fresh one (Fig. 9d). All of the above point to the great stability of $Bi_2Sn_2O_7/TiO_2$ NTAs photoelectrode.

$Bi_2Sn_2O_7$ and TiO_2 have interleaved band structures and can form conventional type II or S-scheme heterojunctions. In the case of conventional type II heterojunctions, the photogenerated e$^-$ and h$^+$ migrate to the CB of TiO_2 and the VB of $Bi_2Sn_2O_7$, respectively (Fig. S10). In this case, the E_{CB} value of TiO_2 (-0.69 eV) is also more negative than that of $O_2/^•O_2^-$ (-0.33 eV vs NHE) [55], and the photogenerated e$^-$ accumulated on the CB of TiO_2 have the ability to reduce O_2, which can generate $^•O_2$

with O_2 by transferring to the counter electrode under the action of an external circuit. However, the h$^+$ accumulated in the VB of $Bi_2Sn_2O_7$ are incapable of generating $^•OH$ with H_2O because the E_{VB} value of $Bi_2Sn_2O_7$ (1.03 eV) is more negative than that of $H_2O/^•OH$ (2.27 eV vs NHE) [56], and the above results are not consistent with active species capture experiments. To further prove the above conclusions, we carried out PEC experiments using pure TiO_2 NTAs, $Bi_2Sn_2O_7/TiO_2$ NTAs, and $Bi_2Sn_2O_7$ coated on FTO as photoanodes, respectively. As previously stated, NBT can be acted as an indicator of $^•O_2^-$, which can react with O_2 to form purple formazan precipitates, leading to a decrease in the intensity of the absorption peak of NBT at 259 nm. As shown in Fig. S11a, as expected,
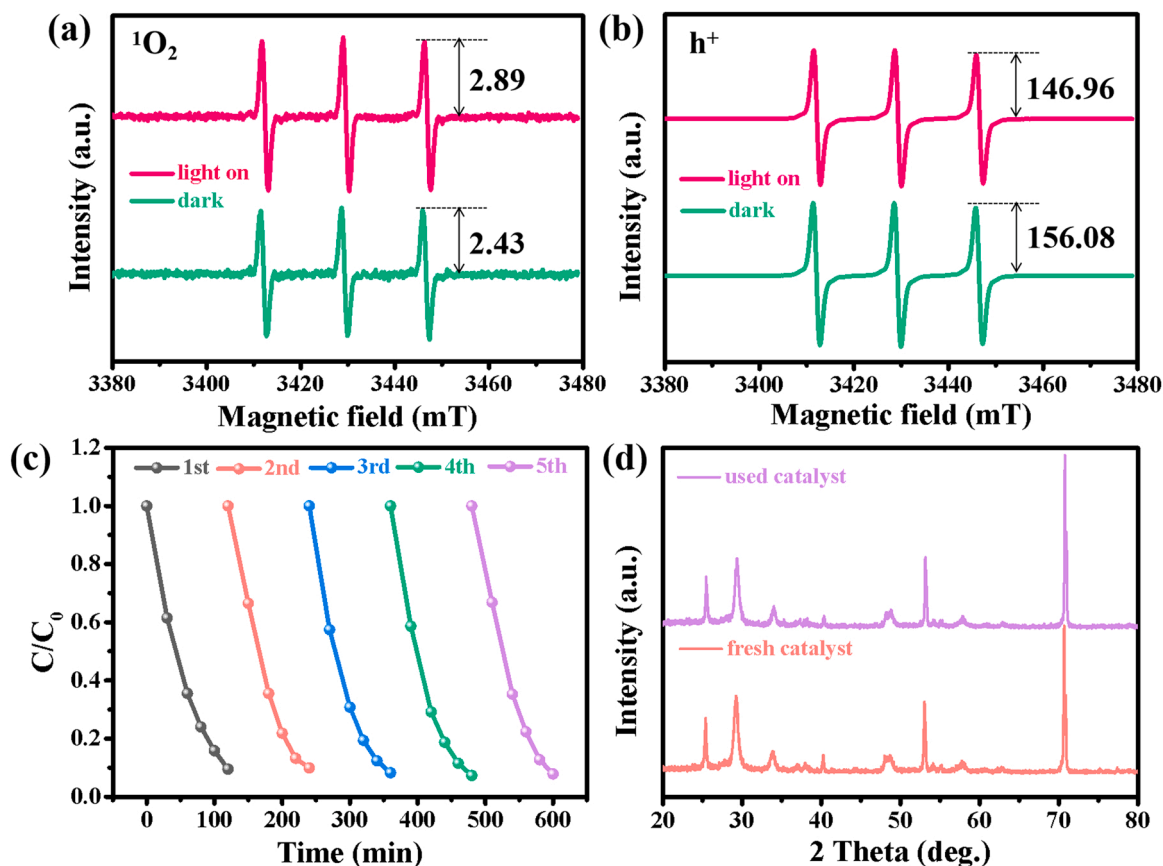
Fig. 9. ESR spectra of (a) DMPO-$^1O_2$ adduct and (b) TEMPO-h$^+$ adduct for $Bi_2Sn_2O_7/TiO_2$ NTAs photoelectrode; (c) Recycling tests; (d) XRD patterns of $Bi_2Sn_2O_7/TiO_2$ NTAs photoelectrode before and after PEC process.

the absorption values of NBT were both reduced after 30 min because the CB edge potential of $Bi_2Sn_2O_7$ (−1.55 eV) and TiO_2 (−0.69 eV) was more negative than the $O_2/{}^\bullet O_2^-$ reduction potential (−0.33 eV), and the reduction of $Bi_2Sn_2O_7/TiO_2$ NTAs composites was more significant compared to TiO_2, indicating that more ${}^\bullet O_2^-$ was generated by $Bi_2Sn_2O_7/TiO_2$ NTAs under the operation of PEC.

In addition, since p-phthalic acid (TA) can react with ${}^\bullet OH$ to form highly fluorescent 2-Hydroxyterephthalic acid (TAOH), TA was chosen as the probe molecule for ${}^\bullet OH$, and the fluorescence intensity of TAOH
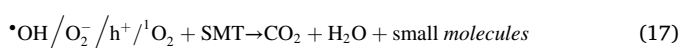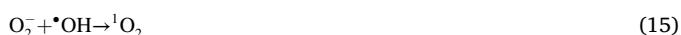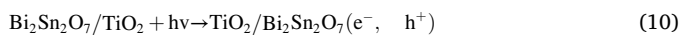
was measured at 425 nm under 315 nm excitation wavelength. As seen in Fig. S11b, the PL peaks centered at 425 nm increased after 60 min of reaction with both $Bi_2Sn_2O_7/TiO_2$ NTAs and TiO_2 NTAs as photoanodes, indicating that ${}^\bullet OH$ were generated, due to the E_{VB} value of TiO_2 (2.39 eV) is more positive than $H_2O/{}^\bullet OH$ (2.27 eV vs NHE). However, no significant elevation in the PL spectrum was observed with $Bi_2Sn_2O_7$ coated on FTO as the photoanode, indicating that no ${}^\bullet OH$ radicals were produced, which was because the E_{VB} value of $Bi_2Sn_2O_7$ (1.03 eV) was more negative than $H_2O/{}^\bullet OH$ (2.27 eV vs NHE).
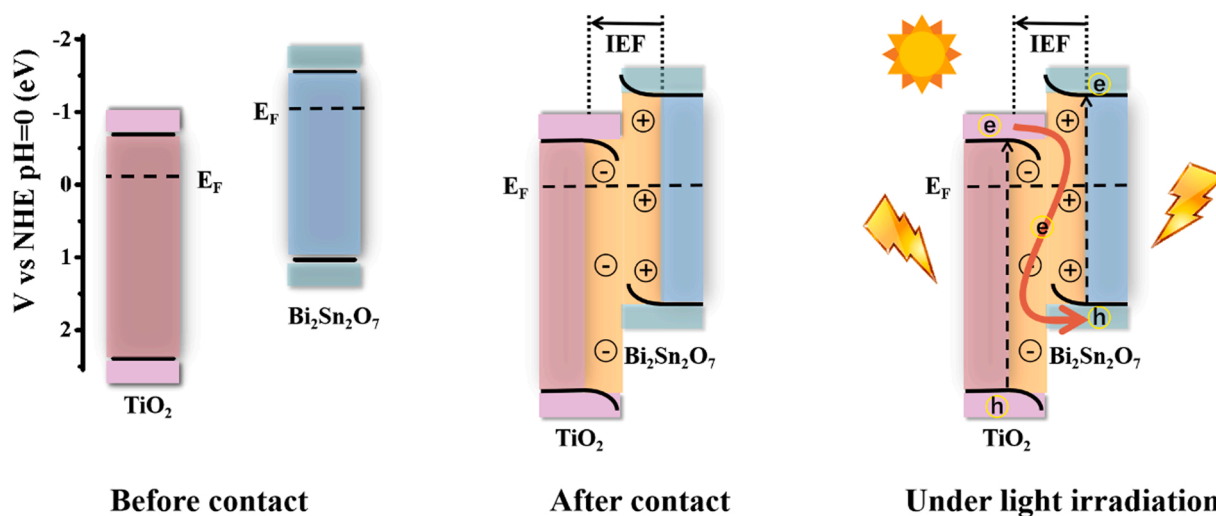
Scheme 2. Schematic illustration of $Bi_2Sn_2O_7/TiO_2$ NTAs heterojunction: IEF-induced charge transfer, separation, and the formation of S-scheme heterojunction under light irradiation.

According to the above analysis, the photogenerated e⁻ and h⁺ accumulate in the VB of $Bi_2Sn_2O_7$ and VB of TiO_2, respectively, and $Bi_2Sn_2O_7$ and TiO_2 are indeed formed as S-scheme heterojunction, which ensures that the whole system has a higher reduction potential to generate free radicals.

The possible separation mechanism of the charge carriers of S-scheme heterojunction $Bi_2Sn_2O_7/TiO_2$ NTAs in the PEC process was elucidated in Scheme 2. Theoretical calculations demonstrated that the Fermi level of $Bi_2Sn_2O_7$ is higher than that of TiO_2, and after the encounter between the two phases, the electrons of $Bi_2Sn_2O_7$ QDs will be shifted toward TiO_2 NTAs until the Fermi levels reach equilibrium, as demonstrated by XPS analysis, an IEF will be established at the interface pointing from $Bi_2Sn_2O_7$ QDs to TiO_2 NTAs. With the aggregation of electrons, the band edge of TiO_2 bends downward, while $Bi_2Sn_2O_7$ bends upward by losing electrons. Under the illumination, the electrons of TiO_2 and $Bi_2Sn_2O_7$ are simultaneously excited from the VB to the CB, respectively. With the effect of the IEF, the photogenerated e⁻ of TiO_2 NTAs on CB will recombine with the photogenerated h⁺ of $Bi_2Sn_2O_7$ QDs on VB, and the h⁺ of TiO_2 are retained on VB where TiO_2 has a high oxidation potential. Eventually, the photogenerated electrons accumulated in the CB of $Bi_2Sn_2O_7$ will be transferred to TiO_2 by an external circuit and to the counter electrode via Ti foil, augmenting the separation of photogenerated e⁻ - h⁺ pairs. The h⁺ in the VB of TiO_2 and the electrons on the counter electrode are involved in the degradation of SMT as shown in Eqs. (10) - (17):

$$Bi_2Sn_2O_7/TiO_2 + h\nu \rightarrow TiO_2/Bi_2Sn_2O_7(e^-, \quad h^+) \tag{10}$$

$$H_2O + h^+ \rightarrow \ ^\bullet OH + H^+ \tag{11}$$

$$O_2 + e^- \rightarrow ^\bullet O_2^- \tag{12}$$

$$O_2 + 2e^- \rightarrow H_2O_2 \tag{13}$$

$$H_2O_2 + e^- \rightarrow ^\bullet OH \tag{14}$$

$$O_2^- + ^\bullet OH \rightarrow ^1O_2 \tag{15}$$

$$^\bullet O_2^- + h^+ \rightarrow ^1O_2 \tag{16}$$

$$^\bullet OH \Big/ O_2^- \Big/ h^+ / {}^1O_2 + SMT \rightarrow CO_2 + H_2O + small \ molecules \tag{17}$$

4. Conclusions

In summary, the novel $Bi_2Sn_2O_7/TiO_2$ NTAs S-scheme heterojunction realizes efficient synergy between photo and electricity in a PEC process and exhibits superior SMT degradation performance. The elevated ability is attributed to the formation of an intimate interface between $Bi_2Sn_2O_7$ QDs and TiO_2 NTAs favoring electron transport, the improved light-harvesting capability from quantum size effect, lower charge transport resistance, and the establishment of S-scheme heterojunction. The formation of S-scheme heterojunction promotes a more efficient separation of e⁻ - h⁺ pairs while maintaining a high redox capacity to be able to produce more h⁺ and ROS to degrade pollutants. Experimental studies and DFT confirm the presence of IEF directed from $Bi_2Sn_2O_7$ to TiO_2 at the interface and elucidate the electron transport mechanism of S-scheme heterojunction. This work proposes a feasible approach for the construction of high-performance heterojunctions and offers a new idea for the preparation of photoanodes in practical wastewater treatment of the PEC process.

Declaration of Competing Interest

The authors declare that they have no known competing financial interests or personal relationships that could have appeared to influence the work reported in this paper.

Data Availability

Data will be made available on request.

Acknowledgments

Appendix A. Supporting information

Supplementary data associated with this article can be found in the online version at doi:10.1016/j.apcatb.2022.122053.

References

[1] S.I. Mulla, Z.K. Bagewadi, B. Faniband, M. Bilal, J.-C. Chae, P.O. Bankole, G. D. Saratale, R.N. Bhargava, D.M. Gurumurthy, Various strategies applied for the removal of emerging micropollutant sulfamethazine: a systematic review, Environ. Sci. Pollut. Res. (2021) 1–15.

[2] Y. Liu, L. Chen, X. Liu, T. Qian, M. Yao, W. Liu, H. Ji, Tuning band structure of graphitic carbon nitride for efficient degradation of sulfamethazine: atmospheric condition and theoretical calculation, Chin. Chem. Lett. 33 (2022) 1385–1389.

[3] Y. Yang, X. Li, C. Zhou, W. Xiong, G. Zeng, D. Huang, C. Zhang, W. Wang, B. Song, X. Tang, Recent advances in application of graphitic carbon nitride-based catalysts for degrading organic contaminants in water through advanced oxidation processes beyond photocatalysis: a critical review, Water Res. 184 (2020), 116200.

[4] F. Li, W. Zhao, D.Y. Leung, Enhanced photoelectrocatalytic hydrogen production via Bi/BiVO₄ photoanode under visible light irradiation, Appl. Catal. B: Environ. 258 (2019), 117954.

[5] A.A. Nada, B.O. Orimolade, H.H. El-Maghrabi, B.A. Koiki, M. Rivallin, M. F. Bekheet, R. Viter, D. Damberga, G. Lesage, I. Iatsunskyi, Photoelectrocatalysis of paracetamol on Pd-ZnO/N-doped carbon nanofibers electrode, Appl. Mater. Today 24 (2021), 101129.

[6] B.O. Orimolade, B.N. Zwane, B.A. Koiki, L. Tshwenya, G.M. Peleyeju, N. Mabuba, M. Zhou, O.A. Arotiba, Solar photoelectrocatalytic degradation of ciprofloxacin at a FTO/BiVO₄/MnO₂ anode: Kinetics, intermediate products and degradation pathway studies, J. Environ. Chem. Eng. 8 (2020), 103607.

[7] H. Zhang, G. Chen, D.W. Bahnemann, Photoelectrocatalytic materials for environmental applications, J. Mater. Chem. 19 (2009) 5089–5121.

[8] X. Zhao, L. Guo, B. Zhang, H. Liu, J. Qu, Photoelectrocatalytic oxidation of CuII-EDTA at the TiO₂ electrode and simultaneous recovery of CuII by electrodeposition, Environ. Sci. Technol. 47 (2013) 4480–4488.

[9] X. Long, J. He, J. Zhou, L. Fang, X. Zhou, F. Ren, T. Xu, A review on light-emitting diode based automotive headlamps, Renew. Sust. Energ. Rev. 41 (2015) 29–41.

[10] K. Natarajan, S. Dave, H.C. Bajaj, R.J. Tayade, Enhanced photocatalytic degradation of nitrobenzene using MWCNT/β-ZnMoO₄ composites under UV light emitting diodes (LEDs), Mater. Today Chem. 17 (2020), 100331.

[11] D. Chen, Y. Cheng, N. Zhou, P. Chen, Y. Wang, K. Li, S. Huo, P. Cheng, P. Peng, R. Zhang, Photocatalytic degradation of organic pollutants using TiO₂-based photocatalysts: A review, J. Clean. Prod. 268 (2020), 121725.

[12] S. Riaz, S.J. Park, An overview of TiO₂-based photocatalytic membrane reactors for water and wastewater treatments, J. Ind. Eng. Chem. 84 (2020) 23–41.

[13] Q. Wang, J. Cai, G.V. Biesold-McGee, J. Huang, Y.H. Ng, H. Sun, J. Wang, Y. Lai, Z. Lin, Silk fibroin-derived nitrogen-doped carbon quantum dots anchored on TiO₂ nanotube arrays for heterogeneous photocatalytic degradation and water splitting, Nano Energy 78 (2020), 105313.

[14] B.A. Koiki, B.O. Orimolade, B.N. Zwane, D. Nkosi, N. Mabuba, O.A. Arotiba, Cu₂O on heterojunction TiO₂ nanotube arrays: A heterojunction photoanode for visible light assisted electrochemical degradation of pharmaceuticals in water, Electrochim. Acta 340 (2020), 135944.

[15] Z. Liu, X. Zhang, S. Nishimoto, T. Murakami, A. Fujishima, Efficient photocatalytic degradation of gaseous acetaldehyde by highly ordered TiO₂ nanotube arrays, Environ. Sci. Technol. 42 (2008) 8547–8551.

[16] K.M. Reddy, S.V. Manorama, A.R. Reddy, Bandgap studies on anatase titanium dioxide nanoparticles, Mater. Chem. Phys. 78 (2003) 239–245.

[17] L. Zhang, J. Zhang, H. Yu, J. Yu, Emerging S-Scheme photocatalyst, Adv. Mater. 34 (2022), 2107668.

[18] Q. Li, W. Zhao, Z. Zhai, K. Ren, T. Wang, H. Guan, H. Shi, 2D/2D Bi₂MoO₆/g-C₃N₄ S-scheme heterojunction photocatalyst with enhanced visible-light activity by Au, Load., J. Mater. Sci. Technol. 56 (2020) 216–226.

[19] F. Zhao, W. Li, Y. Song, Y. Fu, X. Liu, C. Ma, G. Wang, X. Dong, H. Ma, Constructing S-scheme Co_3O_4-C_3N_4 catalyst with superior photoelectrocatalytic efficiency for water purification, Appl. Mater. Today 26 (2022) 101390.

[20] H. Kunioku, M. Higashi, O. Tomita, M. Yabuuchi, D. Kato, H. Fujito, H. Kageyama, R. Abe, Strong hybridization between Bi-6s and O-2p orbitals in Sillén–Aurivillius perovskite Bi_4MO_8 X (M= Nb, Ta; X= Cl, Br), visible light photocatalysts enabling stable water oxidation, J. Mater. Chem. A 6 (2018) 3100–3107.

[21] Z. Ai, Y. Huang, S. Lee, L. Zhang, Monoclinic α-Bi_2O_3 photocatalyst for efficient removal of gaseous NO and HCHO under visible light irradiation, J. Alloy Compd. 509 (2011) 2044–2049.

[22] H. Huang, X. Han, X. Li, S. Wang, P.K. Chu, Y. Zhang, Fabrication of multiple heterojunctions with tunable visible-light-active photocatalytic reactivity in BiOBr-BiOI full-range composites based on microstructure modulation and band structures, ACS Appl. Mater. Inter. 7 (2014) 482–492.

[23] J. Yu, A. Kudo, Effects of structural variation on the photocatalytic performance of hydrothermally synthesized $BiVO_4$, Adv. Funct. Mater. 16 (2006) 2163–2169.

[24] L. Li, Y. Yang, G. Li, L. Zhang, Conversion of a Bi nanowire array to an array of Bi-Bi_2O_3 core-shell nanowires and Bi_2O_3 nanotubes, Small 2 (2006) 548–553.

[25] H. Fu, L. Zhang, W. Yao, Y. Zhu, Photocatalytic properties of nanosized Bi_2WO_6 catalysts synthesized via a hydrothermal process, Appl. Catal. B Environ. 66 (2006) 100–110.

[26] H. Guo, C.G. Niu, L. Zhang, X.J. Wen, C. Liang, X.G. Zhang, D.L. Guan, N. Tang, G.-M. Zeng, Construction of direct Z-scheme AgI/$Bi_2Sn_2O_7$ nanojunction system with enhanced photocatalytic activity: accelerated interfacial charge transfer induced efficient Cr (VI) reduction, tetracycline degradation and Escherichia coli inactivation, ACS Sustain. Chem. Eng. 6 (2018) 8003–8018.

[27] M. Chen, D.W. Goodman, Catalytically active gold: from nanoparticles to ultrathin films, Acc. Chem. Res. 39 (2006) 739–746.

[28] M. Ye, J. Gong, Y. Lai, C. Lin, Z. Lin, High-efficiency photoelectrocatalytic hydrogen generation enabled by palladium quantum dots-sensitized TiO_2 nanotube arrays, J. Am. Chem. Soc. 134 (2012) 15720–15723.

[29] Z. Yan, W. Wang, L. Du, J. Zhu, D.L. Phillips, J. Xu, Interpreting the enhanced photoactivities of 0D/1D heterojunctions of CdS quantum dots/TiO_2 nanotube arrays using femtosecond transient absorption spectroscopy, Appl. Catal. B: Environ. 275 (2020) 119151.

[30] R. Liu, W.D. Yang, L.S. Qiang, J.F. Wu, Fabrication of TiO_2 nanotube arrays by electrochemical anodization in an NH_4F/H_3PO_4 electrolyte, Thin Solid Films 519 (2011) 6459–6466.

[31] C. Zhou, C. Lai, P. Xu, G. Zeng, D. Huang, C. Zhang, M. Cheng, L. Hu, J. Wan, Y. Liu, In situ grown AgI/$Bi_{12}O_{17}Cl_2$ heterojunction photocatalysts for visible light degradation of sulfamethazine: efficiency, pathway, and mechanism, ACS Sustain. Chem. Eng. 6 (2018) 4174–4184.

[32] Y.Y. Yang, X.G. Zhang, C.G. Niu, H.P. Feng, P.Z. Qin, H. Guo, C. Liang, L. Zhang, H. Y. Liu, L. Li, Dual-channel charges transfer strategy with synergistic effect of Z-scheme heterojunction and LSPR effect for enhanced quasi-full-spectrum photocatalytic bacterial inactivation: new insight into interfacial charge transfer and molecular oxygen activation, Appl. Catal. B Environ. 264 (2020) 118465.

[33] G. Kresse, J. Furthmüller, Efficiency of ab-initio total energy calculations for metals and semiconductors using a plane-wave basis set, Comp. Mater. Sci. 6 (1996) 15–50.

[34] G. Kresse, J. Furthmüller, Efficient iterative schemes for ab initio total-energy calculations using a plane-wave basis set, Phys. Rev. B 54 (1996) 11169.

[35] J.P. Perdew, K. Burke, M. Ernzerhof, Generalized gradient approximation made simple, Phys. Rev. Lett. 78 (1997), 1396-1396.

[36] M. Jia, Z. Yang, H. Xu, P. Song, W. Xiong, J. Cao, Y. Zhang, Y. Xiang, J. Hu, C. Zhou, Y. Yang, W. Wang, Integrating N and F co-doped TiO_2 nanotubes with ZIF-8 as photoelectrode for enhanced photo-electrocatalytic degradation of sulfamethazine, Chem. Eng. J. 388 (2020), 124388.

[37] Y. Yan, H. Yang, Z. Yi, X. Wang, R. Li, T. Xian, Evolution of Bi nanowires from BiOBr nanoplates through a $NaBH_4$ reduction method with enhanced photodegradation performance, Environ. Eng. Sci. 37 (2020) 64–77.

[38] X. Chen, B. Zhou, S. Yang, H. Wu, Y. Wu, L. Wu, J. Pan, X. Xiong, In situ construction of an SnO_2/g-C_3N_4 heterojunction for enhanced visible-light photocatalytic activity, RSC Adv. 5 (2015) 68953–68963.

[39] S. Sun, H. Ding, L. Mei, Y. Chen, Q. Hao, W. Chen, Z. Xu, D. Chen, Construction of SiO_2-TiO_2/g-C_3N_4 composite photocatalyst for hydrogen production and pollutant degradation: insight into the effect of SiO_2, Chin. Chem. Lett. 31 (2020) 2287–2294.

[40] S.J. Liu, L.Y. Chen, C.Y. Liu, H.W. Fang, J.H. Hsieh, J.Y. Juang, Physical properties of polycrystalline Cr-doped SnO_2 films grown on glasses using reactive dc magnetron co-sputtering technique, Appl. Surf. Sci. 257 (2011) 2254–2258.

[41] F. Xu, K. Meng, B. Cheng, S. Wang, J. Xu, J. Yu, Unique S-scheme heterojunctions in self-assembled TiO_2/$CsPbBr_3$ hybrids for CO_2 photoreduction, Nat. Commun. 11 (2020) 1–9.

[42] H. Wang, W. Zhang, X. Li, J. Li, W. Cen, Q. Li, F. Dong, Highly enhanced visible light photocatalysis and in situ FT-IR studies on Bi metal@defective BiOCl hierarchical microspheres, Appl. Catal. B Environ. 225 (2018) 218–227.

[43] Y. Wu, C. Cao, C. Qiao, Y. Wu, L. Yang, W. Younas, Bandgap-tunable phosphorus-doped monolayer graphene with enhanced visible-light photocatalytic H_2-production activity, J. Mater. Chem. C. 7 (2019) 10613–10622.

[44] W. Wang, P. Xu, M. Chen, G. Zeng, C. Zhang, C. Zhou, Y. Yang, D. Huang, C. Lai, M. Cheng, Alkali metal-assisted synthesis of graphite carbon nitride with tunable band-gap for enhanced visible-light-driven photocatalytic performance, ACS Sustain. Chem. Eng. 6 (2018) 15503–15516.

[45] H.Y. Xu, Z.H. Yang, G.M. Zeng, Y.L. Luo, J. Huang, L.K. Wang, P.P. Song, X. Mo, Investigation of pH evolution with Cr (VI) removal in electrocoagulation process: proposing a real-time control strategy, Chem. Eng. J. 239 (2014) 132–140.

[46] P. Song, Z. Yang, G. Zeng, X. Yang, H. Xu, L. Wang, R. Xu, W. Xiong, K. Ahmad, Electrocoagulation treatment of arsenic in wastewaters: a comprehensive review, Chem. Eng. J. 317 (2017) 707–725.

[47] M.A. Urynowicz, In situ chemical oxidation with permanganate: assessing the competitive interactions between target and nontarget compounds, Soil Sediment Contam. 17 (2007) 53–62.

[48] F. Hayati, A.A. Isari, B. Anvaripour, M. Fattahi, B. Kakavandi, Ultrasound-assisted photocatalytic degradation of sulfadiazine using MgO@CNT heterojunction composite: effective factors, pathway and biodegradability studies, Chem. Eng. J. 381 (2020), 122636.

[49] Y. Yue, P. Zhang, W. Wang, Y. Cai, F. Tan, X. Wang, X. Qiao, P.K. Wong, Enhanced dark adsorption and visible-light-driven photocatalytic properties of narrower-band-gap Cu_2S decorated Cu_2O nanocomposites for efficient removal of organic pollutants, J. Hazard. Mater. 384 (2020) 121302.

[50] J. Jia, D. Li, X. Cheng, J. Wan, X. Yu, Construction of graphite/TiO_2/nickel foam photoelectrode and its enhanced photocatalytic activity, Appl. Catal. A: Gen. 525 (2016) 128–136.

[51] Y. Hu, Q. Niu, Y. Wang, Y.N. Zhang, G. Zhao, Highly efficient removal mechanism of dimethyl phthalate over an economical 3D {001}TiO_2/Ti photoelectrode with enhanced photoelectrocatalytic activity and long service life, Appl. Catal. B Environ. 285 (2021), 119812.

[52] H. Wang, Y. Liang, L. Liu, J. Hu, W. Cui, Highly ordered TiO_2 nanotube arrays wrapped with g-C_3N_4 nanoparticles for efficient charge separation and increased photoelectrocatalytic degradation of phenol, J. Hazard. Mater. 344 (2018) 369–380.

[53] W. Liao, Y. Zhang, M. Zhang, M. Murugananthan, S. Yoshihara, Photoelectrocatalytic degradation of microcystin-LR using Ag/AgCl/TiO_2 nanotube arrays electrode under visible light irradiation, Chem. Eng. J. 231 (2013) 455–463.

[54] M.S. Koo, K. Cho, J. Yoon, W. Choi, Photoelectrochemical degradation of organic compounds coupled with molecular hydrogen generation using electrochromic TiO_2 nanotube arrays, Environ. Sci. Technol. 51 (2017) 6590–6598.

[55] W.K. Jo, T.S. Natarajan, Facile synthesis of novel redox-mediator-free direct Z-Scheme $CaIn_2S_4$ marigold-flower-like/TiO_2 photocatalysts with superior photocatalytic efficiency, ACS Appl. Mater. Inter. 7 (2015) 17138–17154.

[56] Y. Du, X. Liu, Q. Wang, L. Yu, L. Chu, M. Sun, Metal free benzothiadiazole-diketopyrrolopyrrole-based conjugated polymer/g-C_3N_4 photocatalyst for enhanced sterilization and degradation in visible to near-infrared region, J. Colloid Interface Sci. 608 (2022) 103–113.